Microstructure and oxidation resistance of relaxed epitaxial nickel thin films grown on (100)- and (110)-SrTiO3 substrates by pulsed laser deposition

Gauthier Lefevre, Sébastien Saitzek, Florent Blanchard, Anthony Ferri, Pascal Roussel, Rachel Desfeux, Adlane Sayede

Microstructure and Oxidation Resistance of Relaxed Epitaxial Nickel Thin Films Grown on (100)- and (110)-$SrTiO_3$ substrates by Pulsed Laser Deposition

Gauthier Lefevre[a], Sébastien Saitzek[a], Florent Blanchard[a], Anthony Ferri[a], Pascal Roussel[a], Rachel Desfeux[a], Adlane Sayede[a]

a Univ. Artois, CNRS, Centrale Lille, ENSCL, Univ. Lille, UMR 8181, Unité de Catalyse et Chimie du Solide (UCCS), F-62300 Lens Cedex

Abstract

The relaxed epitaxial growth of Ni thin films has been successfully performed on both (100)- and (110)-oriented $SrTiO_3$ substrates by pulsed laser deposition, as revealed by pole figures realized by X-ray micro-diffraction and rocking curves measurements. In the case of Ni films deposited on (110)-$SrTiO_3$ substrate, advanced microstructural X-Ray Diffraction study (ω-scans vs. φ and Reciprocal Space Maps) evidences the existence of two domains disoriented with respect to the substrate crystallographic axes (both in-plane with + 5° and - 5° tilts (±1°) and out-of-plane with + 3.7° and – 3.7° tilts (±0.1°), respectively). Besides the lattice misfit constraints, the layer orientation can also be controlled by strain/surface energy balance. The surface energies modeling of nickel makes it possible to explain the observed growth, by a low surface energy anisotropy. Furthermore, the high temperature oxidation resistance of the films under air has been studied by *in-situ* high-temperature X-ray diffraction. While the results show the formation of a NiO oxide layer which retains the initial orientation of the Ni film, the Ni corrosion temperature are found to be 500°C and 375°C when grown on (100)- and (110)-$SrTiO_3$ substrates, respectively. Such a high corrosion temperature for Ni films grown on (100)-$SrTiO_3$ substrate is linked to their highest density, as observed by atomic force microscopy.

1. Introduction

Since last decades, nickel and nickel oxide thin films have been widely used because of their remarkable properties. On one hand, nickel is a ferromagnetic transition metal (Curie Temperature (T_c) is 631 K)[1] with face centered cubic (fcc) structure ($Fm\bar{3}m$),[2] it has a low electrical resistivity and a good resistance to oxidation.[3] Thanks to its interesting properties, together with its moderate cost, popularity of nickel is increasing. Nickel has recently shown benefits in a wide range of domains, from catalysis[4] to energy storage devices.[5] Particularly, nickel magnetization makes it useful in several topical fields: magnetic resonance imaging,[6] photo thermal conversion,[7] nanotechnology, spin-controlled electronic devices.[8, 9] Its magnetic

properties originates from the spin polarization of the *3d* electrons, which are very sensitive to the local environment and then, are strongly influenced by crystallinity, surface morphology and structure.[10]

On the other hand, nickel oxide (NiO) is an antiferromagnetic insulator (Neel Temperature (T_N) is 524 K)[11] with NaCl-type structure and is semi-transparent.[12] It has an excellent chemical stability and has the particularity of becoming a p-type semiconductor with a tunable wide band gap when its composition changes from stoichiometry by vacancies, interstitial or doping.[13] NiO thin films are therefore also attractive for various electronic applications: p-type transparent conducting films,[14] electrochromic display devices,[15, 16] Oxide resistive Random Access Memory (OxRAM) for the data storage applications[17] or dielectric materials in the cross-shaped Metal-Dielectric-Metal (MDM) structures.[18] Again, quality and properties of NiO thin films with respect to their formation process is of important interest.[19] Thermal oxidation of Ni metal thin films was shown as an attractive technique to obtain NiO films with interesting properties.[20-22]

To the best of our knowledge, there is no report on the synthesis of textured Ni thin film grown on $SrTiO_3$ substrates by pulsed laser deposition (PLD) and on their oxidation evolution in air.

The elaboration of metallic thin films is challenging by PLD. Indeed, unlike oxides, growth rates are relatively low and it is often preferred to use techniques such as RF magnetron sputtering and thermal evaporation for growth of metal thin films due to a faster deposition rate. The low deposition rate can be explained by several parameters such as the reflectance[23] and the thermal properties[24] of the materials used. In the case of metals, the reflectance is generally higher than for oxides and the ratio between metal/oxide reflectance is more accentuated for higher wavelengths. Thus, at 248 nm, the nickel reflectance is 0.459[25] while most oxides are highly absorbent at this wavelength. Therefore, the electromagnetic radiation can be strongly reflected, requiring large laser-beam intensities to compensate for the reflection losses (threshold ablation increase).[26] The thermal diffusivity is also greater for metals than for oxides (usually a factor of 10).[5] So, if the penetration depth of the beam is much smaller than the thermal diffusion length (which is the case for metals), the energy of the absorbed laser beam contributes to an increase in the target's temperature to the detriment of plasma formation and thus the growth rate.[26] In addition, surface diffusion coefficient (D_S) is also an important parameter on the layer growth. Indeed, during the relaxation time between pulses, the distance d which corresponds to the travel of an adatom before a new plume is calculated from the

following relationship: $d = \sqrt{D_s t}$ (where t is the time between pulses). If the *d* value is low, for a high concentration of atoms arriving on the surface of the substrate, these latter will be almost immobile, thus favoring the clustering probability and consequently the growth of the layer.[27] The parameters described above i.e. high reflectivity, high thermal diffusivity and high surface diffusion coefficient make metals non-preferred candidates for PLD mainly due to their low deposition rates or high ablation thresholds. Despite, this technique presents advantages such as particular growth modes compared to others deposition techniques and the possibility of producing complex hetero-structures. PLD allows the deposition of a metal layer and a complex oxide in the same process and therefore with a good quality interface, essential for nano-electronic applications. The elaboration of nickel thin films by PLD are very scarce. Among these, we could mention the growth of Ni thin film on glass substrate,[28] the elaboration of monocrystalline thin films in rock salt[29] and the epitaxial growth of Nickel thin film on α-Al_2O_3[30,31] or MgO[32] substrates. In this work, we are interested in the growth of nickel thin films by PLD on oriented (100)- and (110)-$SrTiO_3$ substrates. We will study more particularly the influence of the pressure and the substrate temperature in order to obtain epitaxial nickel films. A part dedicated to surface energies calculations will explain the preferential crystallographic orientations obtained. We will also be interested in the oxidation of these films through *in-situ* measurements performed by X-ray diffraction to quantify the corrosion resistance of thin films.

2. Experimental Section

Ni thin films were elaborated by PLD using a KrF excimer laser (COMPexPro series 102 - Coherent) with a wavelength of 248 nm and a pulse duration of 20 ns. The energy pulse was fixed at 200 mJ i.e. a value of density energy (fluence) of about 2 J/cm^2. The target used is a commercial nickel cylinder (1.0" Dia. x 0.125" Thick - Kurt J. Lesker – purity: 99.99%). The target-to-substrate distance and the repetition rate were 35 mm and 3 Hz, respectively. During this work, only air pressure in the chamber (P), number of laser pulses (N) and temperature of the sample holder were studied. Ni thin films were grown on (100)- and (110)-$SrTiO_3$ substrates. At room temperature, $SrTiO_3$ substrates crystallizes in cubic perovskite structure with $Pm\bar{3}m$ space group and with a lattice parameter of 3.905 Å (Crystal GmbH, Germany). With the aid of an ultrasonic bath, all substrates were cleaned in acetone and then in ethanol for 5 minutes. Each substrate was fixed to a heater plate using silver paste for a good thermic contact.

All thin films were characterized by X-Ray Diffraction (XRD) and X-Ray Reflectometry (XRR) using a SmartLab Rigaku High Resolution diffractometer equipped with a 9 kW rotating anode X-ray generator ($\lambda K_{\alpha 1}$=1.54059 nm).The X-ray beam was made parallel with a Göbel mirror and monochromatized with a double Ge (220) monochromator. In this study, all the (ω–2θ) scans were performed in the range of 20 to 90°, with a step size of 0.02° and with a speed of 2°/min. This configuration was also used to achieve rocking-curves. Pole Figures were carried out without monochromator and using a microdiffraction (μXRD) setup with a focused-spot size of 400 μm diameter. The XRR measurement were performed with a step size of 0.01° in the range of 0 to 4° for 2θ and using automatic attenuator.

The surface morphology and roughness of the films were locally determined by Atomic Force Microscopy (AFM) using a commercial microscope (Multimode, Nanoscope V; Bruker) working under environmental conditions. Topography was imaged in AC mode by using silicon nitride ultralever tips.

To get insights on the particular growth of nickel films on $SrTiO_3$ substrate, surface energy (γ) of relaxed and strained surfaces have been calculated at ab initio level. Density functional calculations were carried out using the Vienna Ab initio Simulation Package (VASP),[33-35] together with Projector Augmented-Wave (PAW) potentials.[36,37] The Perdew-Burke-Ernzerhof (PBE) generalized gradient approximation (GGA)[38] was used to evaluate the exchange and correlation energies. PAW potential was used and have [Ar] core (radius 2.3 u.a.) for nickel atoms. To guarantee the reliability of results, an optimization of the cutoff energies as well as the k-point meshes were carried out. Convergence for the total energy was obtained with a 9x9x9 Monkhorst-Pack grid centered at the Ω-point (for bulk optimization), resulting in 35 *k*-points in the irreducible first Brillouin zone and the cutoff energy was set at 700 eV. For surfaces, the *k*-points were reduced or increased proportionally to ensure a similar sampling of the reciprocal spaces. The optimization of structures was done when the force tolerance was lower than 0.01 meV/Å and the energy difference was lower than 10^{-6} eV. Spin-polarization was included throughout calculations. Calculations performed for the bulk metal structures identified a lattice constant of a_{Ni} = 3.517 Å, in very good agreement with experimental (a_{Ni} = 3.520 Å) and theoretical values (a_{Ni} = 3.516 Å).[39] For surface energy calculations, a 1 x 1 surface unit cell model with 10 Å vacuum layer and six periodic metal atom layers was used, since an acceptable convergence of the surface energy (<0.015 mJ/m²) was reached for 6 layers. The surface energy γ is a fundamental property of metallic surfaces and is strongly dependent on surface constraints, induced e.g. by epitaxial growth.[40] In order to shed more light on strain

effects on surface energy anisotropy, biaxial strain distribution has been chosen to investigate the strain effects on the three low-index Ni surfaces $\gamma_{(100)}$, $\gamma_{(110)}$ and $\gamma_{(111)}$. Biaxial strain state consists on an increase or a decrease of in-plane lattice constants within a range of ± 5%. Nickel has a fcc-type structure which is an easy situation for surface energy calculation by the usual equation:[41]

$$\gamma_{(hkl)} = (E^{(hkl)}_{slab} - n\, E_{bulk})/2A$$

where $E^{(hkl)}_{slab}$ is the total energy of the relaxed surface slab of direction (hkl), E_{bulk} is the total energy per atom of the bulk, n is the number of atoms in the slab and A the surface area of the slab model. In the case of strained surface calculations, the same formula is used but $E^{(hkl)}_{slab}$, A as well as E_{bulk} are calculated with respect to the strain state.

3. Results and discussions

First, we studied the influence of pressure in the chamber during growth on the structure obtained. XRD patterns obtained on oriented (100)-$SrTiO_3$ substrates elaborated at 700°C with varying pressure are shown in Figure 1.a. Nickel thin film with fcc structure ($Fm\bar{3}m$) and a (100) preferential orientation is obtained only for the lowest pressure, i. e. 1.10^{-6} mbar. This preferential orientation is interesting because cubic closed packed metals naturally prefer to grow with a (111) orientation, owing to the lowest relative surface energy of {111} planes. For a chamber pressure of 1.10^{-5} mbar, we note the appearance of a bi-phasic Ni / NiO (cubic structure – $Fm\bar{3}m$) mixture with the (100) preferential orientations. Beyond this pressure, only the NiO oxide is observed highlighting a relatively low corrosion pressure. Temperature also plays an important role. Indeed, the oriented film is obtained only when the substrate is heated to 700°C (Figure 1.b). Below this temperature, a polycrystalline thin film is preferred. The line broadening analysis can provide microstructural informations on size and shape of crystallites. The line broadening analysis in 2θ-ω (e.g. its Full Width at Half Maximum (FWHM) or Integral Breadth (β)) quantifies the crystallinity or crystal quality of the thin film (figure 1.c) and allows to determine the vertical coherence length of the crystallites by Scherrer formula.[42,43] The rocking curve (Figure 1.d) is used to determine the mosaic spread by the FWHM measure but also makes it possible to estimate the lateral coherent length of the crystallites. So, similar FWHM in both directions leads to the conclusion of spherical crystallites. In this present case, the crystallite size is calculated to be 17 ± 2 nm (after deconvolution of the instrumental

contribution) and the FWHMs in both directions are quite close, thus we can conclude on the presence of nanocrystallites of spherical shape in Ni / (100)-STO thin films.

To determine if an epitaxial growth or a textured layer takes place, we carried out Pole Figures (PF) in μXRD mode. Figure 2.a shows a PF at 2θ=44.53° corresponding to the {111} reflection of Ni. The analysis was performed by a visual comparison of the measured enhanced pole densities (presented in log scale for the reflection intensity) with calculated spherical projections of $SrTiO_3$ and Ni, using the STEREOPOLE software.[44] The poles observed can be simulated considering a Ni thin film with (001) orientation (blue index) deposited on a (100)-orientated $SrTiO_3$ substrate (red index). A textured layer with random orientation in plane would give a uniform distribution of scattering intensity displaying a ring pattern with or without modulated intensity in PF. But, in this case, we observe a spot pattern. However, the epitaxial relationships that can be deduced from this PF are: $[010]_{Ni}$ // $[010]_{STO}$, $[001]_{Ni}$ // $[001]_{STO}$ and $(100)_{Ni}$ // $(100)_{STO}$. This result is surprising because there is no direct relationship to explain the adaptability of the two structures. Indeed, the lattice parameters of the two structures are too far i.e. a = 3.520 Å and a = 3.905 Å for Ni and $SrTiO_3$, respectively. Therefore, the layer orientation is fairly close of alignment with the substrate in both in-plane and out-of-plane directions. Layer consists of relaxed mosaic blocks and we can conclude that it is an epitaxial thin film with relaxed layer growth. A second PF performed at 2θ=76.45° (figure 2.b), corresponding to the {220} reflection of Ni, confirms the conclusions made. Note that when indexing poles (in the same color code), the presence of poles with a β subscript indicates reflections due to the K_β=1.3921 Å radiation of copper. Indeed, in μXRD mode, the monochromator is not present on the optical line and the convergent mirror does not eliminate completely the K_β component.

Thin nickel films are often used as linear thermistors [45] or ferromagnetic thin film.[46] In order to quantify their resistance to oxidation occurring at high temperature, we carried out a study on Ni(100)/(100)-STO thin film by *in-situ* High Temperature X-ray Diffraction (HT-XRD) under air. This was performed in a temperature range from 50 to 800°C in steps of 25°C and in an angular range of 35° to 85°. The most interesting part is shown in Figure 3. We can highlight that the Ni layer is resistant to HT-oxidation to roughly 500°C (Map realized from XRD patterns vs. annealed temperature presented in figure 3.b makes it easier to see this limit). Beyond this, it completely oxidizes to NiO. Indeed, we note the appearance of a peak at 2θ=43.35° characteristic of nickel oxide. This peak has a high FWHM and this suggests the formation of a nanocrystalline layer of NiO. For a polycrystalline film, Valladares et *al.*[21] have shown that

the oxidation starts around 400°C with the presence of Ni/NiO phase mixture. In the case of textured layer, as prepared in this work, the oxidation takes place at higher temperature towards 500°C.

The same study was carried out on a (110)-$SrTiO_3$ substrate. Figure 4.a shows the influence of the chamber pressure on the film growth. This must be very low (1.10^{-6} mbar) in order to obtain a Nickel thin film with the (110) preferential orientation. Beyond, the film oxidizes leading to the formation of a bi-phasic Ni/NiO mixture. We can note that the growth of the NiO film is performed by maintaining the same direction as the nickel film. Preservation of initial orientation has already been observed in previous studies when NiO thin films are reduce by H_2[31] and when Ni thin films are oxidized in air.[21]

Likewise, a high temperature of 700°C for the substrate is required to grow the film in the (110) direction (Figure 4.b). At lower temperature, no peak is observed but the layer is conductive. This result indicates the presence of nickel in a nanocrystalline or amorphous layer. The line broadening analysis on (110) reflection in 2θ-ω mode (Figure 4.c), shows a FWHM at 0.397° allowing to calculate a size of crystallites of 25 ± 2 nm (after deconvolution of the instrumental contribution). In the case of rocking-curve at φ=90° on Ni(220) reflection (Figure 4.d), the FWHM is more important and therefore the coherent length of crystallites weaker. This result indicates the presence of oblong crystallites within the layer. Nevertheless, we do not observe a single peak when we modify the φ angle. Indeed, for the rocking-curve at φ=0° on Ni(220) reflection (figure 4.d), two peaks separated by 7.4° are highlighted.

In order to elucidate this phenomenon, we have realized a series of rocking curve for different φ values ranging from 0 to 360° (figure 5). Two peaks are observable at φ = 0°/180° while only one peak appears at φ = 90°/270 °. This result can indicate the presence of two domains in the layer. In addition, the two peaks are shifted according to the φ angle, thus indicating that these two domains are not perpendicular each other. We can estimate this shift at about 10° (an angle of 80° between these domains in the plane of the substrate).

A possible interpretation of these results has been made schematically in Figure 5.b. Based on the cubic structure of nickel, the layer must contain two types of crystallites, both of which are misaligned by 3.7° to the normal of the substrate, but also inclined with respect to the [1-10] direction of the substrate. So, at φ = 0°, the two domains diffract separately. Whereas, at φ = 90°, the two domains diffract in the same way. In addition, these domains are not in optimal diffraction position at φ=90° explaining thus the low intensity of reflection observed on θ/ω scans.

It's known that, in the case of metals with fcc structure, several domains can appear because of the presence of coherent twin boundary along [112] direction (resulting from a stacking fault along (111) planes) and/or the boundary grain.[47, 48] We have continued our investigations by performing Pole Figures (PF). Figure 6.a shows a PF at 2θ=44.53° corresponding to the {111} reflection of Ni. Several poles are observed and these can be indexed easily in blue index for Ni with (220) orientation and in red index for $SrTiO_3$ with (110) orientation. These crystallographic projection indicates, in first approximation, the following epitaxial relationships: $[001]_{Ni}//[001]_{STO}$ and $[1\text{-}10]_{Ni}//[1\text{-}10]_{STO}$. However, as before, no adaptation of the two structures can be expected because of the large lattice mismatch. Moreover, the presence of the twin boundary cannot be identified from (111) reflection because it remains unchanged in both domains. Thus, a second PF was performed at 2θ=51.89° (Figure 6.b) highlights a doubling of spots attributed to (020) and (200) reflections (dotted around in Figure 6.b). This confirms the presence of two domains with tilting of the slabs in the plane of the substrate as indicated in Figure 5.b. At this stage more precise epitaxial relations can be given: $[001]_{Ni}$ (titled 5°) // $[001]_{STO}$; $[1\text{-}10]_{Ni}$ (tilted 5°) // $[1\text{-}10]_{STO}$; $(110)_{Ni}$ (titled 3.7°) for the domain 1 (D_1) and $[001]_{Ni}$ (titled -5°) // $[001]_{STO}$; $[1\text{-}10]_{Ni}$ (tilted -5°) // $[1\text{-}10]_{STO}$; $(110)_{Ni}$ (titled -3.7°) for domain 2 (D_2).

The presence of the two domains is also confirmed by the Reciprocal Space Map performed around the (200) reflection of the nickel (figure 7) where we observe a splitting of the node with an angle of 5.2°, in agreement with the value previously determined by the rocking curve on Ni(220) reflection. Indeed, if along the [1-10] direction ($a_{STO}\sqrt{2}$), the angle is 7.4°, so along the [001] direction (a_{STO}), it has to be $7.4/\sqrt{2}$=5.2°. To finish, the relative position of the nodes corresponds to a fully relaxed Ni structure. Thus, as previously, we can conclude that it is an epitaxial thin film with relaxed layer growth.

For Ni(110)/(110)-$SrTiO_3$ thin film, *in-situ* HT-XRD under air was also carried out in order to study the oxidation. The recording was performed in a temperature range from 50 to 800°C in steps of 25°C and from angular range of 35 to 85°. The most interesting part is shown in Figure 8. We can note that the oxidation takes place around 375°C. This temperature is much lower (125°C less) than that obtained on the Ni (100)/(100)-$SrTiO_3$ thin film highlighting a lower limit of use. Besides, the NiO phase appears at the same time as the disappearance of the nickel phase while maintaining the same preferential orientation on the thin film, as previously observed. This result shows differences in oxidation temperatures along the crystallographic reflections of nickel.

Further structural experiments were carried out by X-Ray Reflectometry (XRR). In particular, the thickness of thin films in the one hand, and the apparent density and roughness of the films in the other hand can be determined by XRR technique. This method involves monitoring the intensity of the monochromatic X-Ray beam reflected by the thin film at grazing angle. For an angle less than the critical angle (θ_c), a total reflection occurs. But beyond this critical angle, the reflection of the different interfaces induces interference fringes (usually called Kiessig fringes[49]) more pronounced if there is a noticeable difference in terms of electron density between the substrate and the layer.[50]

In the X-rays range, the complex refractive is given by n=1-δ+iβ where δ is the dispersion of the X-ray beam and β its absorption. The critical angle (θ_c) can be calculated using the dispersion with following relation: $\theta_c = \sqrt{2\delta}$. The δ term is a function of the material density (ρ), the atomic number of the i atom (Z_i), the atomic weight of the i atom, the atomic ratio of the i atom and the atomic scattering factors of the i atom (f_i' / anomalous dispersion term at the considered wavelength), where i correspond to nature of atom in chemical formula. The critical angle is given by the relation:[51,52]

$$\theta_c = \sqrt{\frac{\lambda^2 r_e}{\pi} N_A \rho \frac{\sum_i x_i (Z_i + f_i')}{\sum_i x_i M_i}} \qquad (1)$$

Where r_e is the radius of an electron (2.818×10^{-15} m) and N_A is the Avogadro number (6.022×10^{23} mol^{-1}). Therefore, by knowing the critical angle and the chemical nature of the deposited compound, it is possible to determine the apparent density of the layer and conversely. Regarding the thickness, this is calculated from the periodic oscillations observed for an angle greater than the critical angle. The θ_m angle corresponding of the maximum of the m-th constructive interference is related to the critical angle by:

$$\theta_m^2 = m^2 \frac{\lambda^2}{4d^2} + \theta_c^2 \qquad (2)$$

Where d is the thickness of the layer. By plotting $\theta_m^2 = f(m^2)$, the slope (α) makes it possible to determine the thickness of the film and the intercept (β) is proportional to the apparent density of the film, according to:

$$d = \frac{\lambda}{2\sqrt{\alpha}} \qquad and \qquad \beta = 2\delta \propto \rho \qquad (3)$$

Finally, the exponential decay of the intensity of the reflected beam informs us of the roughness of the film. The more brutal it is, the more the film has a high roughness.

XRR measurements were performed on both Ni thin films grown on (100) and (110)-$SrTiO_3$ substrates, for two deposition conditions i.e. for N=6000 and 12000 (Figure 9) laser pulses. For N=6000 (Figure 9.a), we observe different thicknesses depending on the orientation of the substrate. These are 15 (0.0025 nm/pulse) and 30 nm (0.005 nm/pulse) for (100)-$SrTiO_3$ and (110)-$SrTiO_3$, respectively (and this despite a deposit in the same run). In addition, the critical angle (θ_c) which is proportional to the apparent density of the film, presents different values depending on the orientation of the substrate. θ_c is equal at 0.38° and 0.28° for an orientation (100) and (110), respectively. Therefore, the layer deposited on (100)-$SrTiO_3$ is more dense than the one deposited on (110)-$SrTiO_3$. This apparent density can be calculated from relation (1) and considering Z= 28, M_{Ni}= 58.69 g/mol and *f'*=-3.0029 at λ=1.540520 Å[53], the values 8.26 and 4.52 g/cm^3 are found for Ni(100)/(100)-$SrTiO_3$ and Ni(110)/(110)-$SrTiO_3$, respectively. This large difference may explain the differences in thickness. Indeed, the layer of greater thickness is the one with the lowest apparent density therefore containing the most porosity.

The theoretical density of Ni is 8.9 g.cm^{-3}, the density calculated for the Ni(100)/(100)-$SrTiO_3$ thin film is quite close, indicating the formation of a dense layer of nickel. This is not the case for the Ni(110)/(110)-$SrTiO_3$ thin film, where the density is almost twice as low (so a very rough or porous film). Since it has already been shown that defect density, grain boundary and low atomic surface density (i.e. 79% surface compacity for (100)-fcc plane versus 56% for (110)-fcc plane) play a deleterious role in oxidation resistance,[54] the difference in oxidation temperature between the two orientations could be related to this density disparity: a less dense and rough film implies a more important surface and in consequence a lower oxidation stability. In addition, the reflectivity can be used to characterize the surface roughness. For a rough surface, the reflectivity falls more sharply than for a perfectly flat surface.[55] In first approximation, this decay follows a law of exponential type according to the relation:

$$R(q) = R_F(q)e^{-q^2\sigma^2} \quad \text{with} \quad q = \frac{4\pi \sin(\theta)}{\lambda} \qquad (4)$$

Where $R_F(q)$ is the Fresnel Reflectivity for a perfect flat surface, q is diffusion vector and σ is roughness (Å). Considering the model above, qualitatively, the layer deposited on an (110)-STO substrate has a roughness higher than that deposited on (100)-STO.

For N=12000 (Figure 9.b), only the layer deposited on (100) -STO gives oscillations which makes it possible to calculate a thickness of 30 nm confirming the deposition rate of 0.0025

nm/pulse estimated previously. Moreover, the nickel film deposited on (110) must have a higher roughness than that achieved to N = 6000 because oscillations can't be identified. Finally, we also note a convergence of the critical angles between the two substrates when the number of laser pulses increases and therefore, a noticeable increase in apparent density. The Ni layers being deposited simultaneously, the differences observed between the both substrates, can be explained by the specific arrangement of the atoms during the deposit process, by variations in the sticking coefficients and/or the self-sputtering effects which would be function of the substrate crystallographic orientation.

The surface morphology was investigated on nanoscale by using AFM on as-deposited and annealed (800°C under air) Ni thin films for a deposition time of N=12000 laser pulses. Figure (10.a) illustrates the AFM surface topography of the as-deposited epitaxial Ni (100) thin film. The oriented thin film revealed a nanostructured and rather smooth surface with RMS roughness of 5.7 nm as measured on 5×5 μm² scan area. It is constituted of large grains with irregular shape while smallest ones have near rectangular shapes with additional facets. One can estimate an average lateral size of about 200 nm for grains that are covering 90% of the surface. In addition, all grains exhibit an extremely flat top with sub-nanoscale roughness.

From the simultaneously recorded phase image of the AFM-AC mode (supplementary files), one can perceive clearly that valleys between nickel plateaus are flat and very different in term of contrast, leaving no doubt that the $SrTiO_3$ substrate surface is observed. Hence the approximately 30 nm distance (average height) separating the grain boundaries hollows from grains surfaces can be seen as the film thickness. From previous observations, a dense three-dimensions growth was noticed and the global surface was then principally flat with a thickness of 30 nm; it agrees perfectly on one hand with film thickness deduced from XRR oscillations and on the other hand with nickel bulk-like density calculated from critical angle.

In contrast, as-deposited epitaxial Ni (110) thin film (figure 10.b) exhibits 3d-features with rectangular bases and uniform dimensions. Such growth of nickel thin film with oblong shapes has already been seen on MgO substrate by Tanaka et *al.*[56] and previously deduced from our structural experiments (see figure 4d). Moreover, it can be noticed that rectangular bases have two preferential orientations with tilt angle slightly different from 90° (see inset of figure 10.b). This deviation from the right angle could arise from the different domains identified by XRD analysis. The RMS roughness is of about 12.3 nm, which is twice the value measured for the Ni (100) film. Again, these results are agreeing with the low density and high roughness obtained by XRR measurements.

In addition, on the substrate (110)-$SrTiO_3$, we can distinguish a growth with cubic or rectangular islands compatible with the Stranski-Krastanov or Volmer-Weber growth.[57] This mode of growth, with the presence of cubic and rectangular clusters, has already been observed by M. Tanaka on nickel thin films synthesized by electron beam.[58] These shapes have been explained by a low energy surface favoring partial wetting and the coexistence of these two forms are also explained by the proximity of the values of interface bonding energies for both interfaces, i. e. $\gamma_{\text{bonding cubic}} \sim 1.98$ and $\gamma_{\text{bonding rectangular}} \sim 2.15$ [J/m^2].[58]

Concerning annealed samples, the surface topography patterns of nickel thin films on both substrates (figures 10.c and 10.d) consist of granular-like structure. Even if dense rounded nanostructured grains are more visible on (100)-$SrTiO_3$ substrate, NiO surfaces on both substrates look similar compared to as-deposited films. This similitude is expected since thermal oxidation starts at the surface and is consequently more influenced by the film nature than the substrate.[59] The RMS roughness of both NiO films has increased and is about 20.0 nm, this increase is due to the elevated final annealed temperature.[60]

In the case of fcc metals, it's well known that natural growth with a (111) orientation is preferred thanks to the lowest surface energy of the closed packed {111} plane.[61] Table 1 lists the calculated values of $\gamma_{(hkl)}$ and relaxation Δd_{12} in the first layer spacing for Ni surfaces; results are in good agreement with other theoretical works and in accordance with experimental values.

The surface energy anisotropies of Ni low-index could then give indications on growth of the layer. The wider the anisotropy, the more difficult it is to obtain the concerned orientation. This can help to explain disparities between fcc-metals films. Table 2 presents a comparative study of different metals anisotropies. A previous study of A. J. Francis et *al.*[27] demonstrates that (100) epitaxial growth on perovskite surfaces was more easily stabilized on copper (Cu) than on platinum (Pt). Indeed, a deposition temperature of 300°C was enough to obtain a single (100) crystallinity of Cu film on (100)-$SrTiO_3$ compared to 600°C for a moderate quality epitaxial Pt film. At metal melting temperature (T_M), surface energies converge to fully isotropic liquid state, explaining why surface energy anisotropy is temperature-dependent in the way that increase of temperature lowers the anisotropy. So they highlighted that the intrinsic low surface energy anisotropy of Cu, relative to Pt, corroborates this facilitated growth of Cu (100) contrary to Pt (100). Since equivalent experimental method and substrate were used in the present study, our clear (100) epitaxy of Ni films occurring at 600°C, that is to say in between temperature of epitaxial orientation of Cu and Pt, is in agreement with the sequence of calculated anisotropies $\gamma_{(100)}/\gamma_{(111)}$ (Cu < Ni < Pt).

Table 1. Calculated surface energies $\gamma_{(hkl)}$ (J/m²) and relaxation Δd_{12} (%) of Ni low-index

	This work		Hong et *al.*[63]		Zhang et *al.*[64]	
	GGA (6 layers)		GGA (7 layers)		(broken-bond model)	(Linear fitting method)
	$\gamma_{(hkl)}$	Δd_{12}	$\gamma_{(hkl)}$	Δd_{12}	$\gamma_{(hkl)}$	$\gamma_{(hkl)}$
Ni(100)	2.23	-3.5	2.23	-3.5	2.26	2.25
Ni(110)	2.30	-10	2.29	-11	2.40	2.31
Ni(111)	1.93	-1.2	2.02	-1.3	1.96	1.95

Polycrystalline experimental values: γ = 1.94[65]– 2.05[66] J/m²

Table 2. Calculated values of $\gamma_{(100)}/\gamma_{(111)}$ for selected fcc metals

Cu	Ni	Pt	Method & ref.
1.12	1.16	1.28	GGA, present work
1.09-1.31		1.15-1.38	Equivalent crystal theory[27]
1.12	1.15	1.24	GGA[a,67]

[a] extrapolated from calculated surface energies

To go further on evolution of surface energy with respect to substrate influence, we applied biaxial strain distribution on Ni surfaces (figure 11a). As similar work on Cu,[62] we also denote that surface energy γ decreases with strong lattice compression or expansion. There is however an asymmetric shape with an opposite trend between Ni (110) and Ni (111) surface energies. The former reached a maximum at ~1% in the compressive side while the latter has its

maximum at a tensile strain of ~2%. Nevertheless, regarding the anisotropy of competing (100) and (110) orientations with respect to the lowest surface energy (i.e. of the dense close packed {111} plane) (figure 11b), the stabilization of energetic orientations is always for the benefit of an in-plane expansive strain.

The calculated anisotropy difference presents the same trend as experimental results wherein alteration of Ni (100) thin film during thermal oxidation occurs at higher temperature than Ni (110) orientation. The relatively high surface energy anisotropy of (110) orientation correspond to a low stability of this surface, which is then more easily oxidized. In addition, this theoretical work provides interesting indications on stability behavior of nickel surfaces under bi-axial strain distribution, even if no constraint was observed in present experimental epitaxial nickel films.

4. Conclusions

Using PLD technique, relaxed epitaxial single nickel phase thin films have been successfully grown on both (100)- and (110)-oriented $SrTiO_3$ substrates. On (100)-oriented $SrTiO_3$ substrate, the interpretation of rocking curves measurements combined with Pole Figures recordings lead to the following crystallographic relationships between the film and the substrate: $[010]_{Ni}$ // $[010]_{STO}$, $[001]_{Ni}$ // $[001]_{STO}$ and $(100)_{Ni}$ // $(100)_{STO}$. On (110)-oriented $SrTiO_3$ substrates, two domains are observed, slightly disoriented (3.7°) with respect to the $(110)_{STO}$ planes. In plane, these two populations are disoriented each other from 10°, i.e. $[001]_{Ni}$ // $[001]_{STO}$ and $[1\text{-}10]_{Ni}$ // $[1\text{-}10]_{STO}$ with tilts of +5° and -5°. The values obtained for misorientations and tiltings are confirmed by the analysis of reciprocal space maps and surface morphology images recorded by AFM. X-ray Reflectometry measurements highlight that thickness of the films grown on (110)-oriented $SrTiO_3$ substrates is higher than for films grown on (100) but with a lowest density. As a result, the thickness goes from simple to double (15 nm to 30 nm) for films grown using 6000 laser pulses on (100)- and (110)-oriented $SrTiO_3$ substrates, respectively. On the other hand, HT-oxidation experiments conducted on the films grown on both oriented substrates, show that for (100)-oriented substrates, Ni is oxidized in NiO at higher temperature than for (110)-oriented substrates (500°C vs 375°C). Such different temperature for oxidation related to the orientation of the film is probably explained by the difference of density, taking into account a less dense film. In the case of (110)-oriented substrates, Ni is easier to oxidize, probably due to the more important density of voids inside. These results are in good agreement with ab initio calculations indicating that the (110) orientation of Ni films corresponds to a

surface with low stability and then to a more easily oxidized surface. These results clearly evidence that the microstructure of Ni thin films, mediated by the crystallographic orientation of the substrate, is a major parameter to control the oxidation temperature of Ni films.

Acknowledgements

Chevreul Institute (FR 2638)", "Ministère de l'Enseignement Supérieur et de la Recherche", "Région Nord Pas-de-Calais", "FEDER" and "C'Nano Nord-Ouest compétence centre" are acknowledged for supporting and funding this work. We acknowledge the Centre de Ressources Informatiques de Lille (CRI) for their computing ressources. Authors would like to thank Cyrille Toulet and Matthieu Marquillie for their help on the High Performance Computing cluster of Université de Lille.

References

1 R. A. Serway, R. J. Beichner and J. W. Jewett, *Physics for scientists and engineers*, Philadelphia : Saunders College Publishing, 5th ed., 2000.
2 A. W. Hull., *Phys. Rev.*, 1917, **10**, 661–696.
3 K. Fueki and J. B. Wagner, *J. Electrochem. Soc.*, 1965, **112**, 384–388.
4 J.-W. Li, T. Li, H.-F. Ma, Q.-W. Sun, W.-Y. Ying and D.-Y. Fang, *Fuel Process. Technol.*, 2017, **159**, 31–37.
5 I. N. Lund, J. H. Lee, H. Efstathiadis, P. Haldar and R. E. Geer, *J. Power Sources*, 2014, **246**, 117–123.
6 H. Gleiter, *Acta Mater.*, 2000, **48**, 1–29.
7 M. E. McHenry and D. E. Laughlin, *Acta Mater.,* 2000, **48**, 223–238.
8 S. Das Sarma, J. Fabian, X. Hu and I. Žutić, *Superlattice Microst.*, 2000, **27**, 289–295.
9 V. V. Atuchin, T. I. Grigorieva, L. D. Pokrovsky, V. N. Kruchinin, D. V. Lychagin and C. V. Ramana, *Mod. Phys. Lett. B*, 2012, **26**, 1150029.
10 J. Tersoff and L. M. Falicov, *Phys. Rev. B*, 1982, **26**, 6186–6200.
11 G. Srinivasan and M. S. Seehra, *Phys. Rev. B*, 1984, **29**, 6295–6298.
12 H.-L. Chen, Y.-M. Lu, J.-Y. Wu and W.-S. Hwang, *Mater. Trans.*, 2005, **46**, 2530–2535.
13 E. Antoini, *J. Mater. Sci.*, 1992, **27**, 3335–3340.
14 I.-M. Chan, T.-Y. Hsu and F. C. Hong, *Appl. Phys. Lett.*, 2002, **81**, 1899–1901.
15 M. Kitao, K. Izawa, K. Urabe, T. Komatsu, S. Kuwano and S. Yamada, *Jpn. J. Appl. Phys.*, 1994, **33**, 6656.
16 A. G and C. Od, *Solid State Ion.*, 2017, **305**, 43–51.
17 K. M. Kim, D. S. Jeong and C. S. Hwang, *Nanotechnology*, 2011, **22**, 254002.
18 I. V. Malikov, V. A. Berezin, L. A. Fomin and G. M. Mikhailov, *Russ. Microelectron.*, 2018, **47**, 181–186.
19 J. H. Oh, S. Y. Hwang, Y. D. Kim, J. H. Song and T. Y. Seong, *Mater. Sci Semicon. Proc.*, 2013, **16**, 1346–1351.
20 P. Mohanty, C. Rath, P. Mallick, R. Biswal and N. C. Mishra, *Physica B Condensed Matter.*, 2010, **405**, 2711–2714.
21 L. D. L. S. Valladares, A. IOnescu, S. Holmes and C. H. W. Barnes, *J. Vac. Sci. Technol. B*, 2014, **32,** 051808.
22 L. Courtade, C. Turquat, C. Muller, J. G. Lisoni, L. Goux, D. J. Wouters, D. Goguenheim, P. Roussel and L. Ortega, *Thin Solid Films*, 2008, **516**, 4083–4092.

23 T. Müller, B. K. Sinha and K. P. Rohr, *Phys. Rev. E*, 2002, **66**, 026403.
24 L. M. Doeswijk, G. Rijnders and D. H. A. Blank, *Appl. Phys. A*, 2004, **78**, 263–268.
25 P. B. Johnson and R. W. Christy, *Phys. Rev. B*, 1974, **9**, 5056–5070.
26 E. Matthias, M. Reichling, J. Siegel, O. W. Käding, S. Petzoldt, H. Skurk, P. Bizenberger and E. Neske, *Appl. Phys. A*, 1994, **58**, 129–136.
27 A. J. Francis, Y. Cao and P. A. Salvador, *Thin Solid Films*, 2006, **496**, 317–325.
28 W. O. Siew, S. S. Yapl, T. K. Yong, C. H. Nee and T. Y. Tou, *Appl. Surf. Sci.*, 2011, **257**, 2775–2778.
29 J. Kacher, K. Hattar, I. M. Robertson, *Mat. Sci. Eng. A*, 2016, **675**, 110–119.
30 Y. Kakehi, S. Nakao, K. Satoh and T. Kusaka, *J. Cryst. Growth*, 2002, **237**–**239**, 591–595.
31 A. Matsuda, S. Akiba, M. Kasahara, T. Watanabe, Y. Akita, Y. Kitamoto, T. Tojo, H. Kawaji, T. Atake, K. Koyama and M. Yoshimoto, *Thin Solid Films*, 2008, **516**, 3873–3876.
32 M. Tachiki, T. Hosomi and T. Kobayashi, *Jpn. J. Appl. Phys.*, 2000, **39**, 1817.
33 G. Kresse and J. Furthmüller, *Comp. Mat. Sci.*, 1996, **6**, 15–50.
34 G. Kresse and J. Furthmüller, *Phys. Rev. B*, 1996, **54**, 11169–11186.
35 J. Hafner, *J. Comp. Chem.*, 2008, **29**, 2044-2078.
36 P. E. Blöchl, *Phys. Rev. B*, 1994, **50**, 17953–17979.
37 G. Kresse and D. Joubert, *Phys. Rev. B*, 1999, **59**, 1758–1775.
38 J. P. Perdew, K. Burke and M. Ernzerhof, *Phys. Rev. Lett.*, 1996, **77**, 3865–3868.
39 M.-L. Bonnet, D. Costa, E. Protopopoff and P. Marcus, *Appl. Surf. Sci.*, 2017, **426**, 788–795.
40 A. Boucherif, N. P. Blanchard, P. Regreny, O. Marty, G. Guillot, G. Grenet and V. Lysenko, *Thin Solid Films*, 2010, **518**, 2466–2469.
41 X. Tian, T. Wang, L. Fan, Y. Wang, H. Lu and Y. Mu, *Appl. Surf. Sci.*, 2018, **427**, 357–362.
42 R. Guinebretière, Microstructural Study in thin films. In *X-ray Diffraction by Polycrystalline Materials*, Wiley Online Books, 2010, Chapter 7, pp. 275–318. Doi: 10.1002/9780470612408.ch7.
43 J. I. Langford and A. J. C. Wilson, J. Appl. Crystallogr., 1978, 11, 102–113.
44 I. Salzmann and R. Resel *, J. Appl. Crystallogr.*, 2004, **37**, 1029–1033.
45 J.-J. Wang, H. Hu and C.-H. Shang, *Thin Solid Films*, 2017, **632**, 28–34.
46 P. Kumar, *Nanoscale Res. Lett.*, 2010, **5**, 1596–1602.
47 S. L. Thomas, A. H. King and D. J. Srolovitz, *Acta Mater.*, 2016, **113**, 301–310.
48 D. N. Lee and H. N. Han, *Recent Developments in the Study of Recrystallization*, 2013, Editor P. Wilson, Chapter 1, Intech.
49 H. Kiessig, *Ann. Phys.*, 1931, **402**, 715–768.
50 M. Yasaka, *The Rigaku Journal*, 2010, **26**, 1.
51 I. Kojima and L. Boquan, The Rigaku Journal, 1999, **16**, 31–42.
52 I. Kojima, B. Li and T. Fujimoto, *Thin Solid Films*, 1999, **355**–**356**, 385–389.
53 A. J. C. Wilson and E. Prince, Eds., *International Tables for Crystallography, Volume C: Mathematical, Physical and Chemical Tables*, Springer Netherlands, 2nd edn., 1999.
54 J. Li, J. W. Mayer and E. G. Colgan, *J. Appl. Phys.,* 1991, **70**, 2820–2827.
55 E. Chason and D. T. Warwick, *MRS Proceedings,* 1990, ***208****, 351.*
56 T. Tanaka, T. Nishiyama, K. Shikada, M. Ohtake, F. Kirino and M. Futamoto, *J. Magn. Soc. Jpn.*, 2010, 21–29.
57 H. Brune, Epitaxial Growth of Thin Films. In Surface and Interface Science, K. Wandelt (Ed.), Chapter 20, 2014, doi:10.1002/9783527680566.ch20
58 M. Tanaka, Appl. Surf. Sci., 2014, **311**, 324-329.
59 J. G. Lisoni, L. Goux, T. Hoffmann, D. E. Diaz-Droguett and M. Jurczak, *Corros. Sci.*, 2012, **59**, 282–289.
60 A. M. López-Beltrán and A. Mendoza-Galván, *Thin Solid Films*, 2006, **503**, 40–44.
61 L. Vitos, A. V. Ruban, H. L. Skriver and J. Kollár, *Surf. Sci.*, 1998, **411**, 186–202.
62 L. He, Y. W. Liu, W. J. Tong, J. G. Lin and X. F. Wang, *Surf. Rev. Lett.*, 2013, **20**, 1350054.
63 S. Hong, Y.-H. Shin and J. Ihm, *Jpn. J. Appl. Phys.*, 2002, **41**, 6142.
64 W.-B. Zhang, C. Chen and S.-Y. Zhang, *J. Phys. Chem. C*, 2013, **117**, 21274–21280.
65 V. K. Kumikov and K. B. Khokonov, *J. Appl. Phys.*, 1983, **54**, 1346–1350.

66 H. Meltzman, D. Chatain, D. Avizemer, T. M. Besmann and W. D. Kaplan, *Acta Mater.*, 2011, **59**, 3473–3483.
67 R. Tran, Z. Xu, B. Radhakrishnan, D. Winston, W. Sun, K. A. Persson and S. P. Ong, *Scientific Data*, 2016, **3**, 160080.

Figures Captions

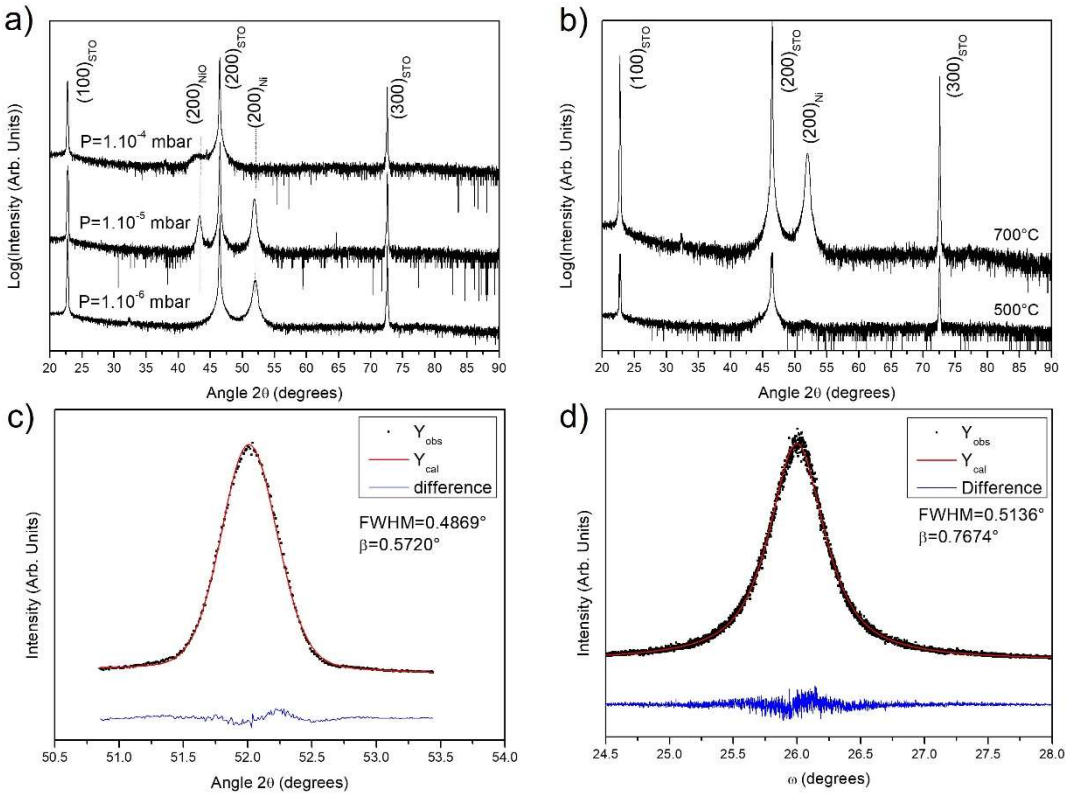

Figure 1. a) XRD patterns of Ni/(100)-$SrTiO_3$ thin films elaborated at 700°C and at different pressure ; b) XRD patterns of Ni films elaborated at 1.10^{-6} mbar and at different temperature; c) Line broadening analysis of (200) reflection and d) Rocking-curve performed on (200) reflection for Ni thin film synthetized at 1.10^{-6} mbar and at 700°C.

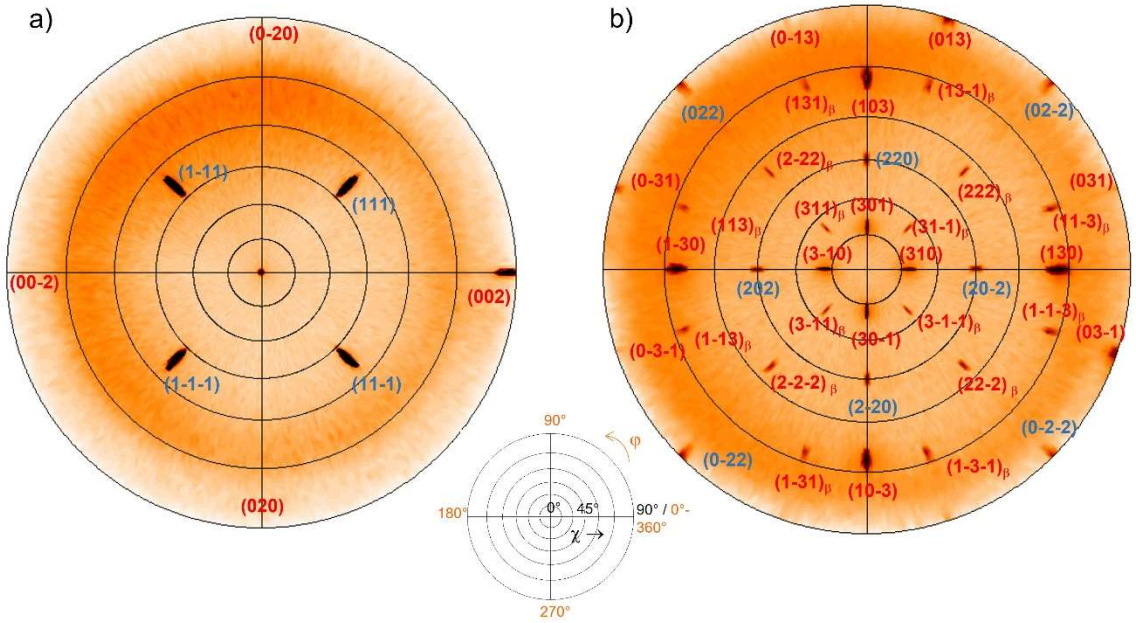

Figure 2. a) Pole Figure obtained at 2θ=44.53°; b) Pole Figure obtained at 2θ=76.45° for Ni thin film grown on a (100)-$SrTiO_3$ by PLD.

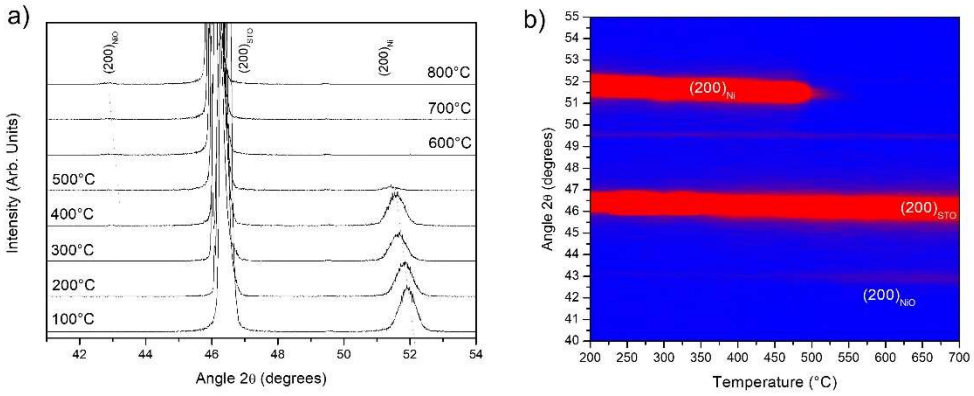

Figure 3. a) XRD patterns of Ni thin films annealed at various temperature under air; b) Maps realized from XRD patterns vs. annealed temperature (200 to 700°C) for Ni thin film deposited on (100)-$SrTiO_3$ substrate under air (streaks correspond to peaks of the heated sample holder).

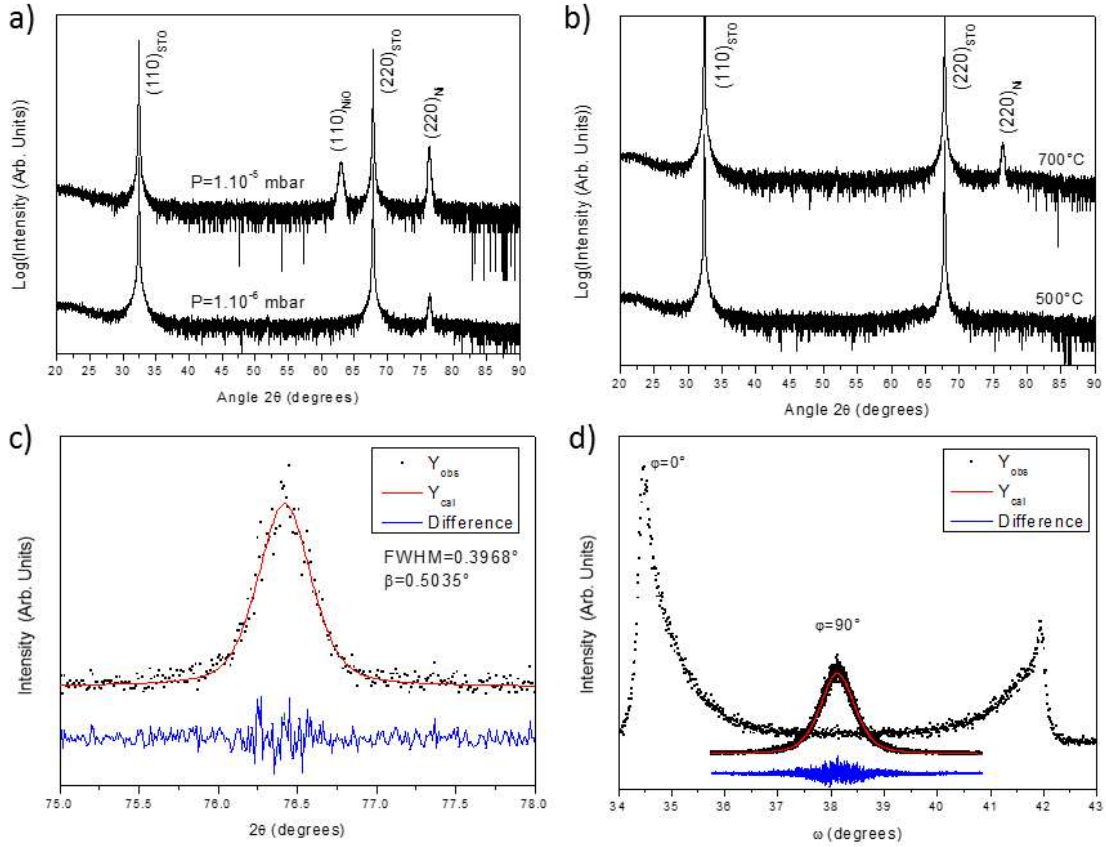

Figure 4. a) XRD patterns of Ni/(110)-$SrTiO_3$ thin films elaborated at 700°C and at different pressure ; b) XRD patterns of Ni films elaborated at 1.10^{-6} mbar and at different temperature; c) Line broadening analysis of (220) reflection and d) Rocking-curve performed on (220) reflection for Ni thin film synthetized at 1.10^{-6} mbar and at 700°C**.**

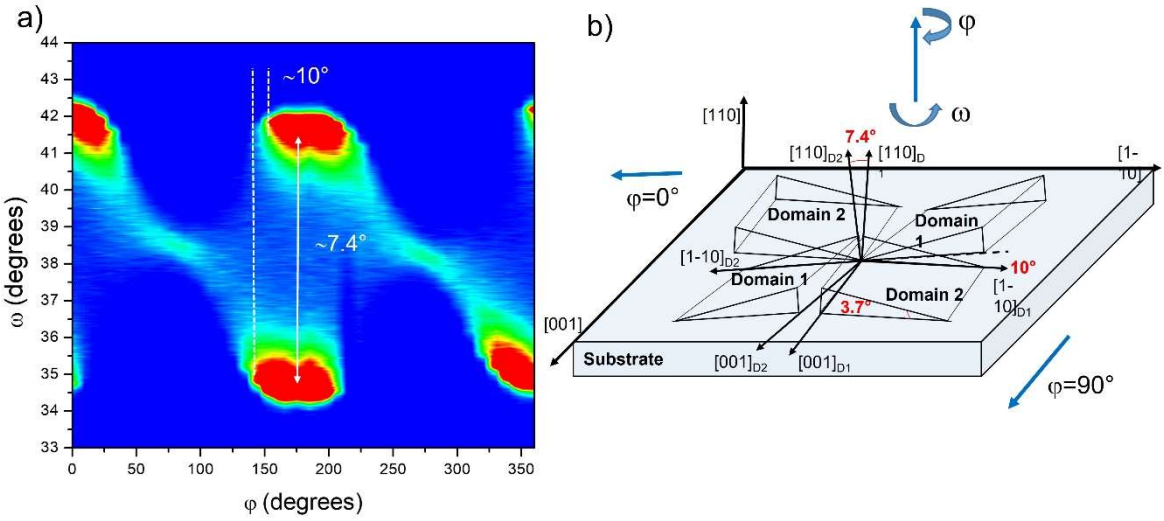

Figure 5. a) ω scans vs. φ for Ni(220) reflection ; b) Schematic positions of the two Ni domains on the(110)-$SrTiO_3$ substrate.

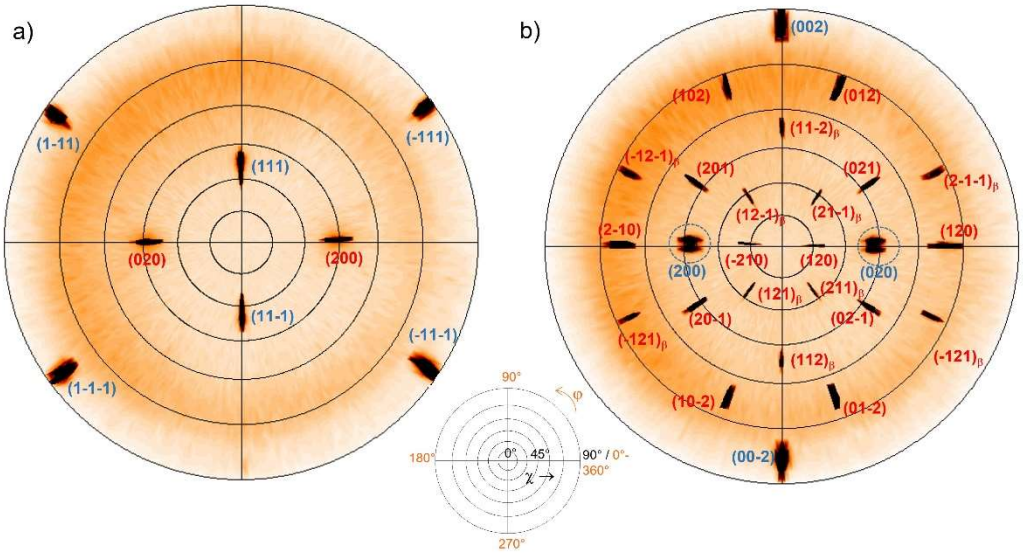

Figure 6. a) Pole Figure obtained at 2θ=44.53°; b) Pole Figure obtained at 2θ=51.89° for Ni thin film grown on a (110)-$SrTiO_3$ by PLD.

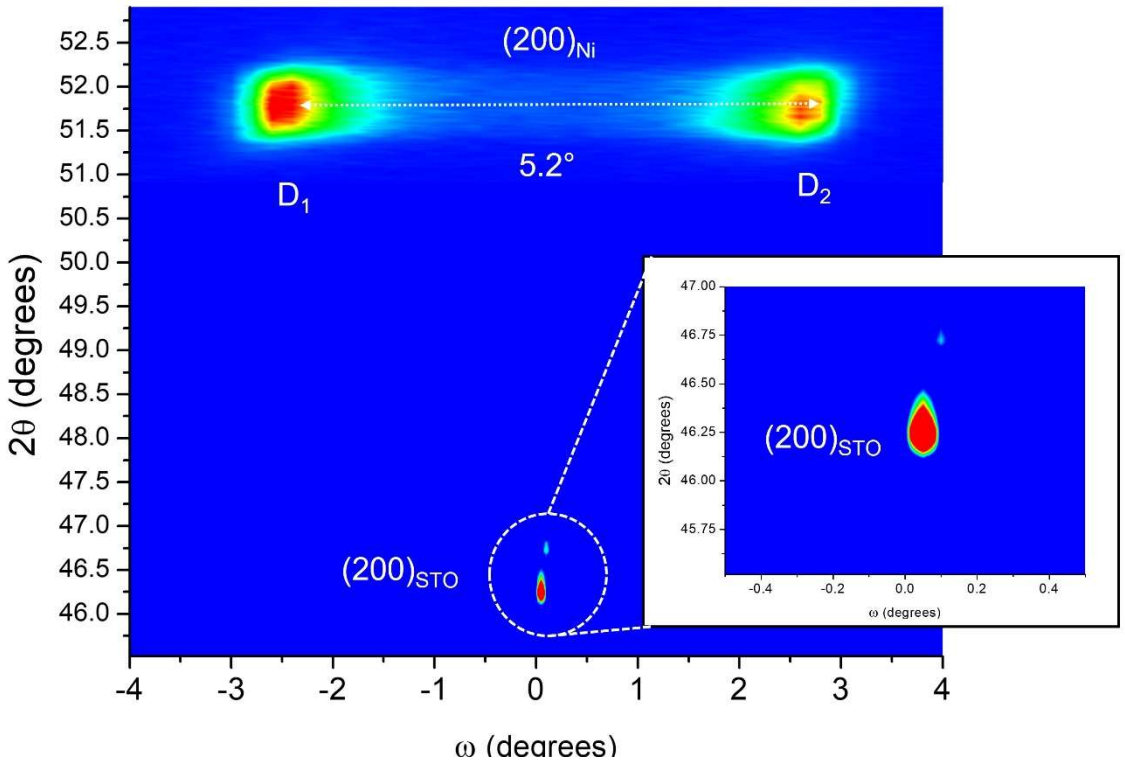

Figure 7. Reciprocal Space Map (RSM) around of (200) reflection of $SrTiO_3$.

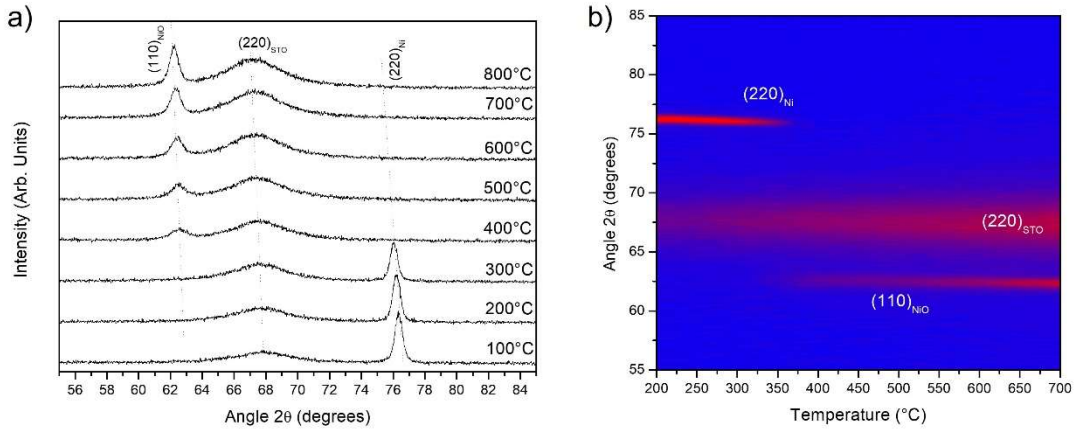

Figure 8. a) XRD patterns of Ni thin films annealed at various temperature under air; b) Maps realized from XRD patterns vs. annealed temperature (200 to 700°C) for Ni thin film deposited on (110)-$SrTiO_3$ substrate under air (streaks correspond to peaks of the heated sample holder).

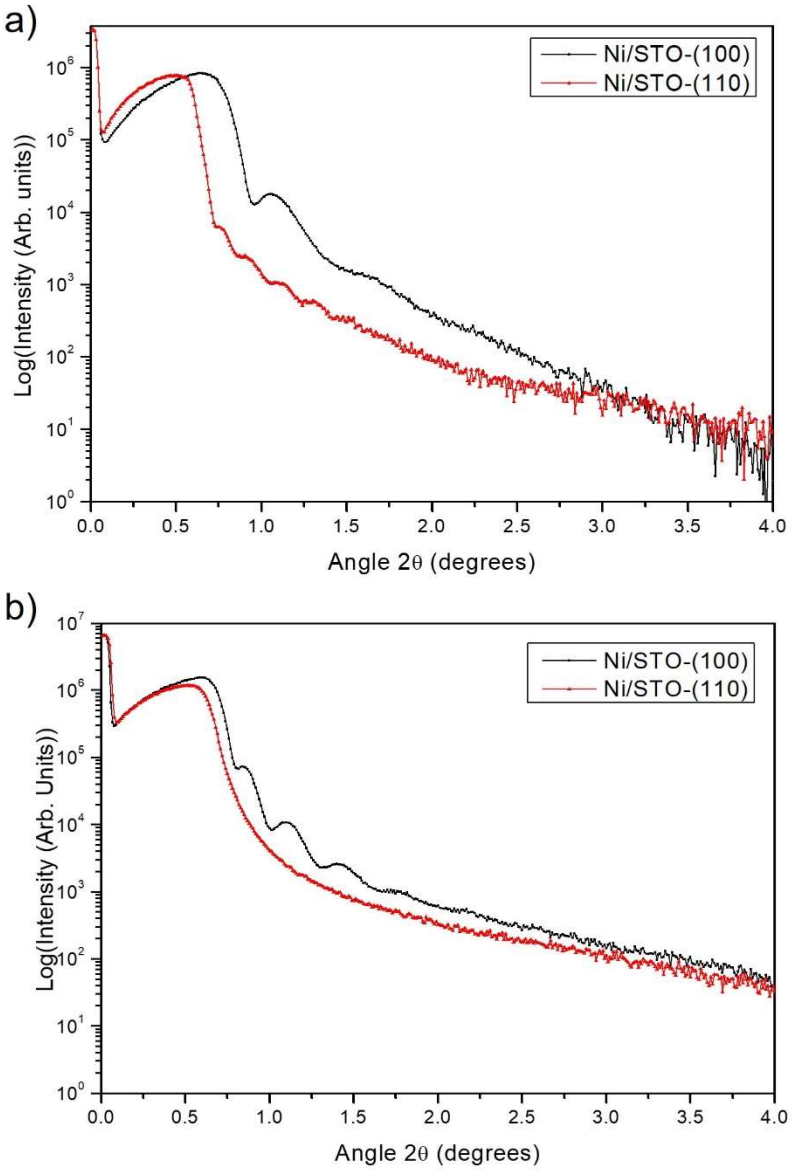

Figure 9. Measured profiles of X-Ray Reflectivity of Ni thin film on (100) and (110)-$SrTiO_3$ substrates: a) for N=6000 laser pulses and b) for N=12000 laser pulses.

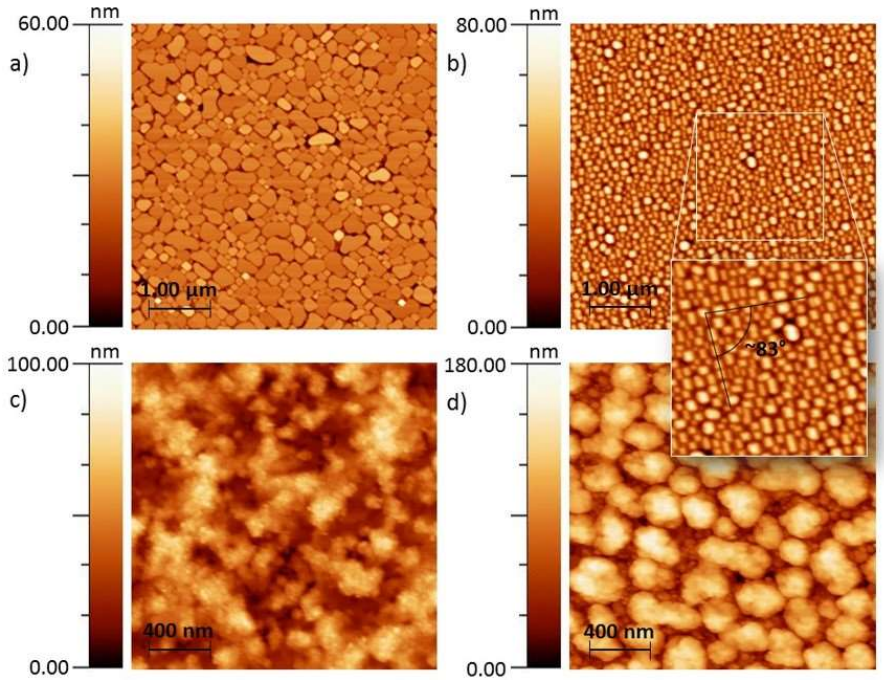

Figure 10. AFM surface topographies of the as-deposited Ni thin film on (a) (100) and (b) (110)-$SrTiO_3$ and annealed (800°C under air) Ni thin film on (c) (100) and (d) (110)-$SrTiO_3$.

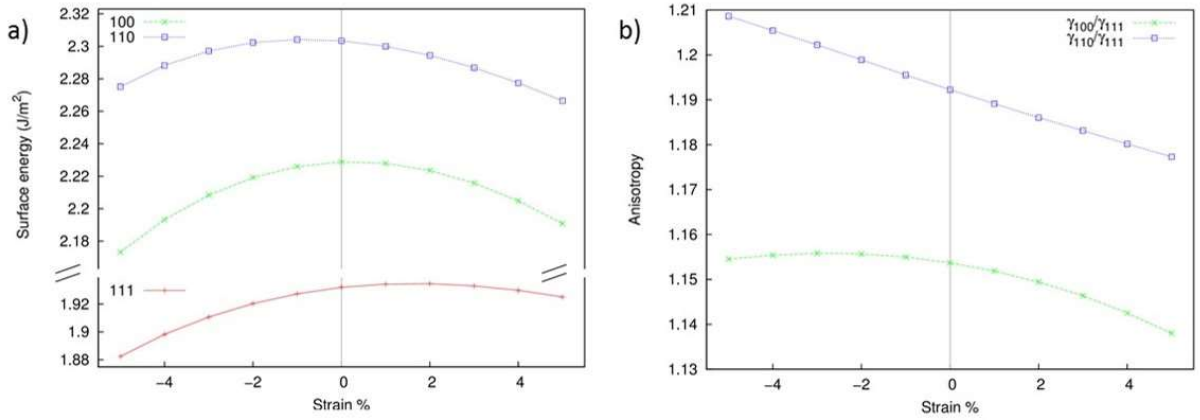

Figure 11. Calculated surface energies γ (a) and anisotropies (b) of Ni low-index surfaces under biaxial strain distribution.